Facile and sustainable synthesis of metal nanoparticles (Ag, Fe, Cu, and Zn) using polyamide and polyhydrazide

Rida Fatima[1] · Nadim Ullah[2] · Uzma Bilal[1] · Hasnain Asghar Khan[1] · Tahani Mazyad Almutairi[3] · Shahroz Saleem[4]

Abstract

In recent years, metal nanoparticles (MNPs) have gained significant research interest owing to their versatile characteristics in diversified applications ranging from catalysis to biomedical sciences. Due to their notable and improved properties such as higher flexibility, facile processability, thermal stability, mechanical strength, and exceptional optoelectrical and magnetic behavior as compared to pristine metal nanoparticles, the polymer mediated nanoparticles have recently drawn interest from both industry and academia. In this novel investigation, we report a sustainable synthesis of Ag, Fe, Cu, and Zn metal nanoparticles using a chemical reduction method using polyamide (PA) and polyhydrazide (PH) matrices. This work is innovative in that it makes use of these polymer matrices for improved MNP synthesis, offering a unique combination of thermal and structural features. The polymers-supported metal nanoparticles were characterized for structural, thermal, optical, chemical, and morphological characteristics using XRD, TGA, UV-Vis, IR spectroscopy, and SEM analysis, respectively. XRD measurements demonstrated a significant rise in the crystallinity index for the produced metal nanoparticles, indicating a significant increase in crystallinity quantitatively. The effective synthesis of nanoparticles with precise attributes was confirmed by UV-Vis spectroscopy, which showed a significant absorption peak in the UV region. The thermogravimetric study suggested an improvement in thermal stability of around 25%. This work offers a flexible and eco-friendly method for synthesizing metal nanoparticles, demonstrating the usefulness of polyamide and polyhydrazide matrices as platforms for the synthesis of nanomaterials for numerous applications including catalysis, electronics, sensors, and biomedical applications.

Graphical Abstract
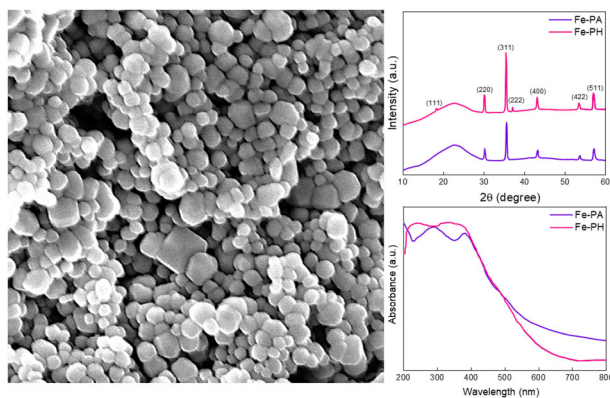
✉ Shahroz Saleem
shahrozkamboh1@gmail.com

1 Institute of Chemical Sciences, Bahauddin Zakariya University, 60000 Multan, Pakistan

2 Institute of Chemical Sciences, University of Peshawar, 25120 Peshawar, Pakistan

3 Department of Chemistry, College of Science, King Saud University, Riyadh 11451, Saudi Arabia

4 School of Materials Science and Engineering, Shaanxi Normal University, Xi'an 710119, PR China

Highlights

- A facile synthesis of metal nanoparticles (Ag, Fe, Cu, and Zn) via chemical reduction approach.
- The nanoparticles of Ag, Fe, Cu, and Zn are formed utilizing polyamide (PA) and polyhydrazide (PH) matrices.
- The synthesized metal nanoparticles exhibited higher crystallinity, better thermal stability, high absorption in UV range.
- This work offers a potential for numerous applications including catalysis, electronics, sensors, and biomedical applications.

1 Introduction

The potential benefits of nanotechnology in various fields including computers, electronics, pharmaceuticals, biology, and catalysis, have made it extremely significant in recent years [1, 2]. Bulk materials can be altered to become stronger, lighter, more resilient, highly reactive, and conductive materials with the help of nanotechnology [3–6]. The rapid advancement in nanotechnology owing to its remarkable potential and ability to manipulate bulk materials at the nanoscale is beneficial. The synthesis of metal nanoparticles (MNP) has received a lot of attention recently due to their unique physicochemical properties and extensive applications in sensing, electronics, adsorbents, health sciences, and catalysis, among other fields [7–9]. Despite different techniques available to synthesize nanoparticles, using polymers as templates or stabilizers has several benefits, including improved stability, regulated size and shape, and simplicity in functionalization [10–12].

Due to their intrinsic qualities and adaptable chemical structures, two distinct groups of polymers, polyamide (PA) and polyhydrazide (PH) have emerged as viable options for the synthesis of MNP [13–16]. The PAs exhibit remarkable mechanical resilience, chemical resistance, and thermal stability due to the presence of amide links in their structures. These characteristics make PAs robust matrices that can be utilized to incorporate MNP by providing a stable environment for nanoparticle-controlled growth [17–19]. On the other hand, PHs, which have functional groups called hydrazides, have unique reactivity and chelating properties favorable in metal ions coordination consequently leading to the formation of nanoparticles [20, 21]. Metal ions can be included in PA or PH matrices via a variety of synthetic procedures, including in situ polymerization, template-assisted approaches, and chemical reduction techniques. By precisely controlling the size, shape, and dispersion of MNP, these techniques enable the tailoring of their properties for desired applications [22–25].

However, the size, shape, and dispersity of the nanoparticles may be less controllable with in situ polymerization. The final product may contain impurities or differ from the original due to side reactions that can occasionally happen during polymerization. Techniques for in-situ polymerization can be more intricate and often require complex equipment or specific conditions. Furthermore, the quality of synthesized nanoparticles can be restricted by the polymer selection and compatibility with the synthesis approach [26–29]. Similarly, the template-assisted approach suffers from the difficulty of removing the template right after the formation of nanoparticles. This can be difficult and may require heat treatments or severe chemical treatments, which might harm the nanoparticles or alter their appearance [30, 31]. Especially for large-scale synthesis, some template materials utilized in template-assisted techniques may be costly or challenging to synthesize [32–35]. The chemical reduction approach, on the other hand, is facile and versatile. The high yield of the final product can be obtained using a chemical reduction technique with strong reproducibility. Furthermore, this is a low-cost approach and has superior control over the shape and size of nanoparticles [36–39]. Advancing MNPs easier to produce while reducing adverse environmental effects requires the development of sustainable synthesis techniques. A viable approach to accomplish this goal is to use polymer matrices as stabilizing agents during the production of nanoparticles. These matrices can improve the mechanical and thermal properties of the resulting MNPs. The use of PA and PH matrices for the synthesis of MNPs is lacking comprehensive investigation, despite their potential benefits. Understanding the full potential of PA and PH in this context is lacking since the majority of studies so far have been on other polymers. This study aims to address this gap by developing a facile and sustainable chemical reduction approach for synthesizing MNP (Ag, Fe, Cu, and Zn) using PA and PH matrices.

The present research deals with the synthesis of MNP (Ag, Fe, Cu, and Zn) using PA and PH via a facile chemical reduction approach. The synthesized polymer-assisted nanoparticles were probed for different structural, thermal, and optical characterizations to examine their distinguished characteristics. The prime objective of this study is to evaluate the improvements in crystallinity, enhancing thermal stability and optimizing the optical characteristics of polymer-mediated nanoparticles. Our research aims to

Table 1 Metal nanoparticles synthesis via polyamide

Nanoparticles	AgNO₃ (g)	Polyamide (g)	DIW	Reducing agent	Stabilizing agent	Thermal treatment	Duration
Silver (Ag)	2 g	2 g	10 ml	Hydrazine monohydrate	Ethanol and polymer	135 °C	35 min
Iron (Fe)	2 g	2 g	10 ml			135 °C	35 min
Copper (Cu)	2 g	2 g	10 ml			135 °C	35 min
Zinc (Zn)	2 g	2 g	10 ml			135 °C	35 min

advance our knowledge of the mechanics behind polymer-mediated nanoparticle formation and to offer new strategies for tailored nanomaterial design and usefulness.

2 Experiment section

2.1 Materials

All chemicals were purchased commercially from Aldrich or Merck. Since they were analytical grade or higher, they did not require additional purification before being used. Silver nitrate (AgNO₃/169.87 g/mol), iron sulfate heptahydrate (FeSO₄·7H₂O/278.02 g/mol), copper sulfate (CuSO₄/159.60 g/mol), zinc chloride (ZnCl₂/136.28 g/mol), 1,3-diaminopropane (NH₂(CH₂)₃NH₂/74.12 g/mol), hydrazine monohydrate (NH₂NH₂·H₂O/50.06 g/mol) and L-tartaric acid (C₄H₆O₆/150.08 g/mol) were procured from Aldrich with purity level >99%. The different solvents utilized in synthesis involve methanol, ethanol, DMF, and acetone which were purchased from Sigma Aldrich and provided by local vendors.

2.2 Synthesis of polyamide (PA) and polyhydrazide (PH)

PA and PH were synthesized separately via direct treatment of tartaric acid with 1,3-diamino propane and hydrazine monohydrate, respectively. At the neutralization point solutions turned a light-yellow color as the acid-base reaction occurred and the temperature of the reaction chamber was increased to 90 °C. After cooling the above solutions, polar solvents (methanol or ethanol) were gradually added to them. A yellow, sticky substance that resembles gel accumulates at the bottom of the reaction flask. The technique produced a sizable yield of product.

2.3 Synthesis of metal (Ag, Fe, Cu, and Zn) nanoparticles with polyamide

2 g of each precursor salt, silver nitrate, iron sulfate hepta hydrate, copper sulfate, and zinc chloride containing 2 g of PA each were dissolved separately in four different beakers containing 10 ml of deionized water (DIW). The mixed

solution of precursor salt and PA was taken in a round bottom flask fitted with a condenser. The precursor solutions were stirred using a magnetic stirrer on a hot plate at a temperature up to 135 °C for 35 min. After heating and stirring the solution, a few drops of hydrazine monohydrate were added as a reducing agent into that solution. The color of the solution changes to light gray, light black, golden brown, and off-white for silver nitrate, iron sulfate, copper sulfate, and zinc chloride precursor solutions, respectively. A few drops of ethanol as a stabilizing agent and the solution of pre-synthesized polymer were added. The mixtures were condensed for 90 min with continuous stirring. Finally, the nanoparticles were washed with DIW, and absolute ethanol followed by vacuum drying at 70 °C for 3 h. The synthesis details are provided in Table 1.

2.4 Synthesis of metal (Ag, Fe, Cu, and Zn) manoparticles with polyhydrazide

2 g of each precursor salt, silver nitrate, iron sulfate hepta hydrate, copper sulfate, and zinc chloride containing 2 g of PH each were dissolved separately in four different beakers containing 10 ml of deionized water (DIW). The mixed solution of precursor salt and PA was taken in a round bottom flask fitted with a condenser. The precursor solutions were stirred using a magnetic stirrer on a hot plate at a temperature up to 135 °C for 35 min. After heating and stirring the solution, a few drops of hydrazine monohydrate were added as a reducing agent into that solution. The color of the solution changes to light gray, light black, golden brown, and off-white for silver nitrate, iron sulfate, copper sulfate, and zinc chloride precursor solutions, respectively. A few drops of ethanol as a stabilizing agent and the solution of pre-synthesized polymer were added. The mixtures were condensed for 90 min with continuous stirring. Finally, the nanoparticles were washed with DIW, and absolute ethanol followed by vacuum drying at 70 °C for 3 h. The synthesis details are provided in Table 2.

2.5 Methods of characterization

The crystallinity of MNP was measured using an X-ray diffractometer (Bruker D8 Advance). The sample used for measurement was in powder form. The surface morphology

of as-synthesized MNP was examined by a scanning electron microscope (VEGA3-Tescan, USA). The optical properties including absorption characteristics of MNP were recorded in a spectrophotometer (Shimadzu 1800, Japan). The surface characterization and chemical composition of MNP were investigated by IR spectrophotometer (BRUKER PLATINUM-ATR). The UV-Vis and IR measurements were performed using a dispersion of MNP. The thermal stability of MNP was investigated by a thermogravimetric (TG) analyzer (DTG-60 Shimadzu, Japan) at a ramp rate of 15 °C/min.

3 Results and discussion

## 3.1 Structural, thermal, optical, and chemical properties of Ag nanoparticles

Figure 1a shows the crystalline structure and phase compositions of pre-synthesized silver nanoparticles. Four unique diffraction peaks (~38°, 44°, 64°, 77°) that match the typical XRD pattern [JCPDS No: 03-0931] correspond to the (111), (200), (220), and (311) planes of the silver crystal, respectively [40]. Compared to JCPDS, the 2θ values obtained from the XRD pattern of Ag NPs are marginally lower. The produced silver nanoparticles are face-centered cubic structures. The result indicates that by addition of polyamide/polyhydrazide and hydrazine monohydrate as reducing agents to the solution reduces the silver nitrate precursor to generate crystallized Ag NPs. Nevertheless, compared to those synthesized with PH, the diffraction peak intensity of the silver nanoparticles synthesized with PA was found to be higher. With Ag-PH samples, a broader diffraction peak was also noted. In XRD patterns, broad peaks usually correspond to smaller crystallite sizes or poor crystallinity. In contrast to Ag-PH, the Ag-PA pattern may indicate more favorable crystallization conditions for silver nitrate, leading to larger crystallites or higher crystallinity. Another cause of the peak broadening could be a structural disorder between the silver nitrate and

Table 2 Metal nanoparticles synthesis via polyhydrazide

Nanoparticles	AgNO$_3$ (g)	Polyhydrazide (g)	DIW	Reducing agent	Stabilizing agent	Thermal treatment	Duration
Silver (Ag)	2 g	2 g	10 ml	Hydrazine monohydrate	Ethanol and polymer	135 °C	35 min
Iron (Fe)	2 g	2 g	10 ml			135 °C	35 min
Copper (Cu)	2 g	2 g	10 ml			135 °C	35 min
Zinc (Zn)	2 g	2 g	10 ml			135 °C	35 min

Fig. 1 Silver (Ag) nanoparticles synthesized from polyamide (PA) and polyhydrazide (PH); XRD patterns (**a**), TGA Curves (**b**), UV-VIS spectra (**c**), and IR spectra (**d**)
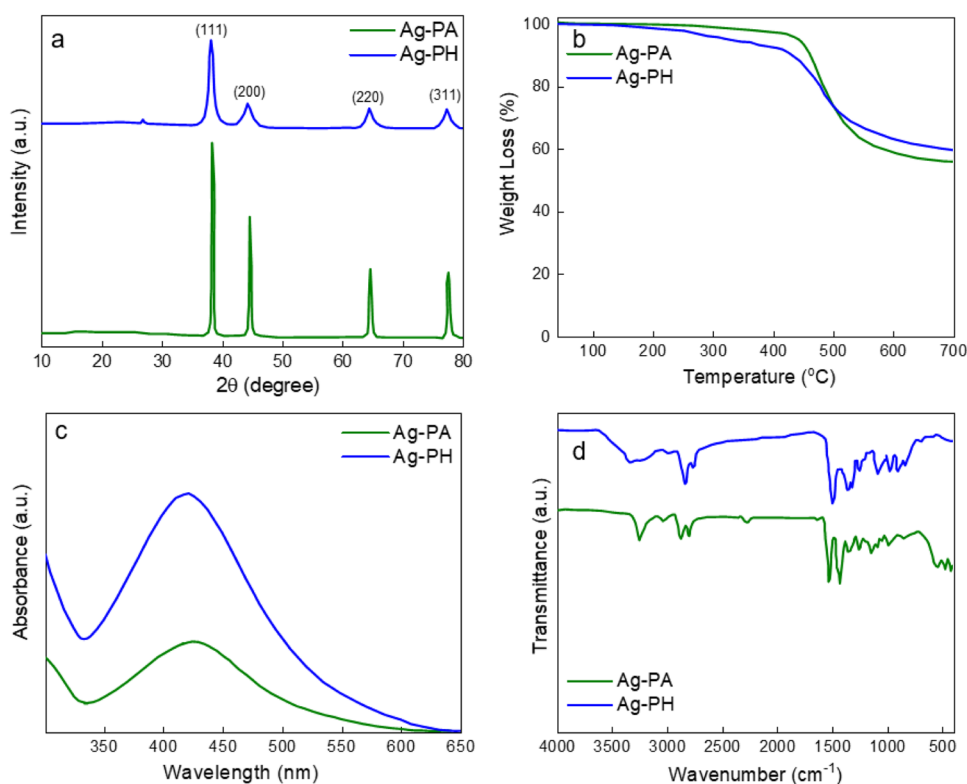
Fig. 2 Iron (Fe) nanoparticles synthesized from polyamide (PA) and polyhydrazide (PH); XRD patterns (**a**), TGA Curves (**b**), UV-VIS spectra (**c**), and IR spectra (**d**)
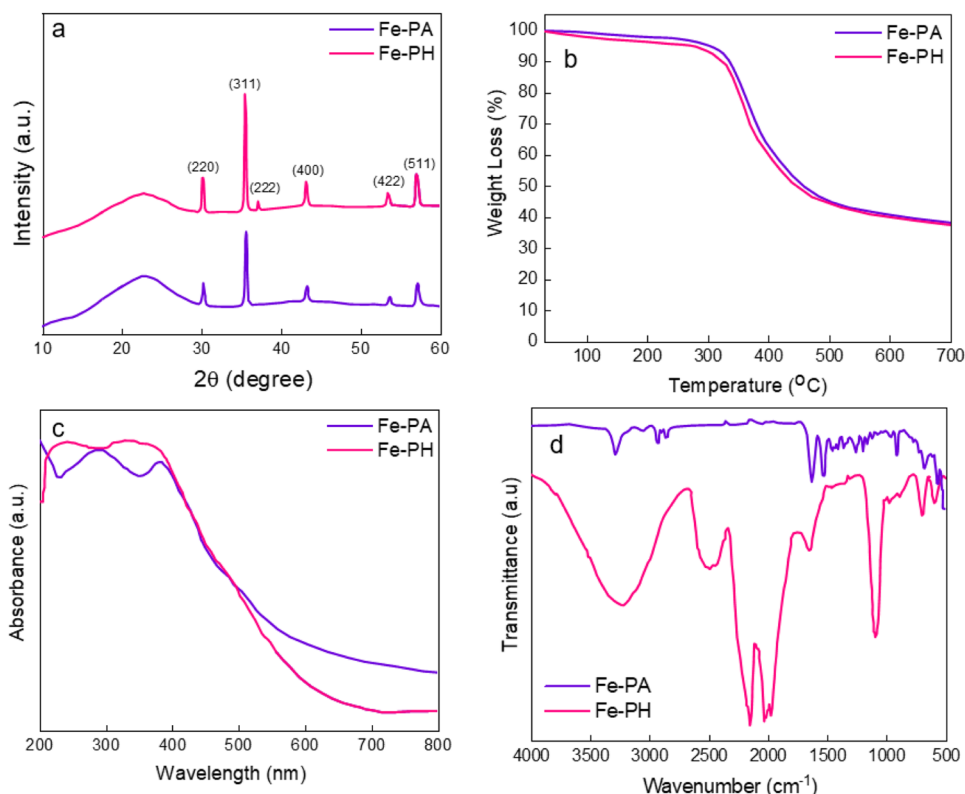
PH, which would distort the crystal lattice [41]. Owing to the amorphous nature of polymers, no diffraction peak corresponding to PA or PH was observed in either of the XRD patterns. To examine the polymer content on the silver nanoparticle surface, thermogravimetric analysis (TGA) was performed on the produced samples in a nitrogen atmosphere. Figure 1b demonstrates that, for Ag-PA and Ag-PH samples, the total weight loss of the silver nanoparticles is less than 4% and less than 8%, respectively, up to 400 °C, demonstrating greater thermal stability of the nanoparticles with polymer matrix. To provide more context, the thermal decomposition of Ag-PA and Ag-PH samples is observed in two stages, the first of which occurs in the range between 40 and 400 °C, and the second of which occurs in the range between 400 and 550 °C. Minor weight loss (less than 10%) happens in the first stage and is caused by dehydration or ethanol evaporation [42]. Polymer matrix decomposition is responsible for the majority of the degradation in both samples above 400 °C. Similar to clean Ag-PH, Ag-PA samples display an analogous decomposition pattern.

The UV-Vis absorbance spectra of the pre-synthesized Ag-PA and Ag-PH nanoparticles are shown in Fig. 1c. The presence of silver nanoparticles was confirmed by the peak of the silver absorption spectra, which can be observed to arise at 425 nm for Ag-PA and 420 nm for Ag-PH samples, respectively. Because of their surface plasmon resonance,

silver nanoparticles have a specific absorption peak in the UV-visible range. The spherical shape of silver nanoparticles is further confirmed by the presence of a single, concentrated corresponding absorption peak [43]. Ag-PA and Ag-PH nanoparticles were subjected to FTIR spectroscopy experiments, as shown in Fig. 1d. The characteristic vibration frequency peaks of Ag-PA are located at 1434 cm^{-1} (NH bending vibration), 2881 cm^{-1} (CH$_2$ stretching), 3258 cm^{-1} (N-H stretching), and 588 cm^{-1} (N-H bending vibration). The vibration frequency of the amine group is slightly shifted from the reported literature in the presence of Ag NPs at the PA surface [44]. This difference might suggest that Ag NPs are forming physical bonds with the amine group of PA. Ag nanoparticles are responsible for the peaks at 433 cm^{-1} and 545 cm^{-1}. However, for the Ag-PH sample, we observed a peak of silver nanoparticles at 568 cm^{-1}. SPR of the silver nanoparticles may be the cause of the minor shift in the peak position in the IR spectra.

3.2 Structural, thermal, optical, and chemical properties of Fe nanoparticles

The XRD analysis was conducted to investigate the crystalline nature of Fe nanoparticles, and the related patterns are displayed in Fig. 2a. The diffraction peaks at $2\theta = 30.19°, 35.43°, 37.15°, 43.17°, 53.44°,$ and $57.03°$ in the XRD data of the as-synthesized sample Fe-PA can be

Fig. 3 Copper (Cu) nanoparticles synthesized from polyamide (PA) and polyhydrazide (PH); XRD patterns (**a**), TGA Curves (**b**), UV-VIS spectra (**c**), and IR spectra (**d**)
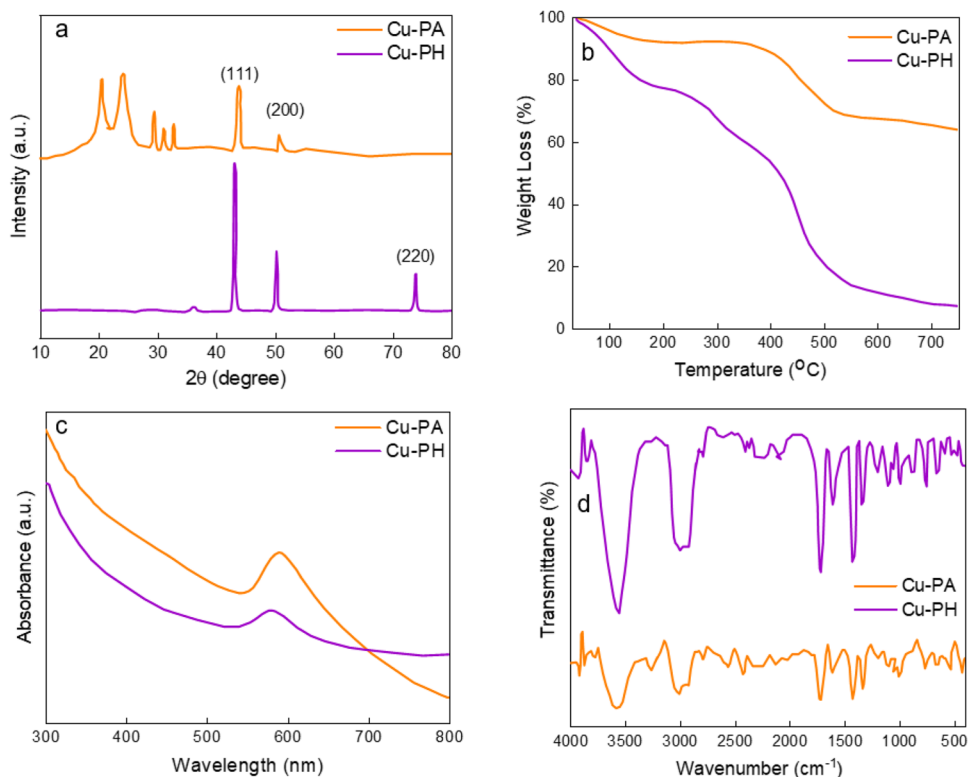
attributed to the (220), (311), (222), (400), (422), and (511) planes of magnetite (Fe_3O_4) nanoparticles, respectively (JCPDS No: 01-1111). This suggests that the magnetite particles in the composites were pure with a cubic spinal structure. The relative intensities and position of the reflection peaks in both samples agree well with the XRD patterns previously reported [45]. Due to the polymer network, both samples exhibit a large peak at $2\theta = 23°$ [46]. However, the peak of the iron nanoparticles did not show up at 18° might be due to the peak of the polymer at 23°.

Figure 2b shows the TG curves of Fe-PA and Fe-PH nanoparticles. The samples' temperature of thermal degradation was typically between 300 and 500 °C. The mere 6% weight loss below °C is indicative of water desorption and minimal monomer residue in the matrix. The two samples displayed comparable patterns of decomposition, and the decomposition at higher temperatures can be linked to polymer decomposition. Fe-PA and Fe-PH samples have a high transparency in visible light and an excellent UV absorption capability, as shown in Fig. 2c. Two abrupt rises show at around 286 nm and 391 nm for the Fe-PA sample, and 240 nm and 340 nm for the Fe-PH sample, respectively. The absorption edge wavelength is shorter than 600 nm, and the absorption increases steadily up to the peak at the wavelength of about 400 nm [47]. These findings imply that polymer-doped nanoparticles cause a significant increase in absorption up to 400 nm and give nanoparticles-based samples the ability to screen against UV radiation and

become transparent in the visible light spectrum. Figure 2d shows the IR spectra of Fe-PA and Fe-PH nanoparticles. The Fe-PA spectrum exhibits a characteristic expansion of the peaks around the 400–700 cm^{-1} absorption bands, which is indicative of Fe-O stretching. Additionally, the peak at 570 cm^{-1} validates the inclusion of Fe_3O_4, while the 908 cm^{-1} is ascribed to amide stretching. The Fe-PH IR spectrum is also displayed in Fig. 2d. Peaks may be seen in the Fe-PH IR spectra at 586 and 693 cm^{-1}. The iron nanoparticle bands at about 586 and 693 cm^{-1} matched the Fe-O bond bending and stretching vibrations that are typical of the crystalline lattice of the magnetite mineral phase, however, the Fe-PH showed a transient, strong peak at 1091 cm^{-1}. O-H stretching at 3236 cm^{-1} was widely exhibited by the Fe-PH nanoparticles due to the presence of O-H in the water or alcohol used to clean the particles. The existence of water was confirmed at 1645 cm^{-1} by the O-H bending absorption band. The C-O stretching absorption bands at 1087 cm^{-1}, which may have resulted from the use of ethanol and water before drying, indicated the presence of O-H in the nanoparticles [48].

3.3 Structural, thermal, optical, and chemical properties of Cu nanoparticles

The XRD patterns of Cu-PA and Cu-PH nanoparticles are displayed in Fig. 3a. It was evident that PA6 had α crystals that matched 19° and 23°. Furthermore, there was good

agreement between the XRD peaks at 43° and 50°, which correspond to the (111) and (200) planes, respectively, supporting the synthesis of Cu nanoparticles in the Cu-PA sample (JCPDS No: 85-1326). In the Cu-PH sample, the XR diffractogram showed peaks at $2\theta = 43°$ (Cu-111), 50° (Cu-200), and 74.13° (Cu-220), which corresponded to the Cu structure. Copper nanoparticles made from PH have higher peak intensities in XRD analysis than copper nanoparticles made from PA, suggesting a reduced degree of crystallinity [49]. The TG curves of the chemically synthesized copper nanoparticles from PA and PH are displayed in Fig. 3b. At first, both samples showed significant weight losses between 40 and 150 °C, which are correlated with the capping agent breakdown and the residual solvent evaporation, respectively [50]. Cu-PH samples have two weight gain stages and one weight gain stage for Cu-PA, respectively, involving copper nanoparticles. For the Cu-PH sample, the first weight increase stage begins at around 150 °C and finishes at about 225 °C. The second weight gain-only stage begins at 300 °C and ends at about 350 °C. The two weight growth stages of copper nanoparticles and the decomposition stages line up. The copper nanoparticles begin to gain weight in the first stage when the polymer begins to lose weight due to decomposition. The copper nanoparticles reach the second weight gain stage when the temperature rises further. Eventually, the copper nanoparticles stop growing in mass and are fully oxidized as the decomposition process ends. Absorption peaks in UV-vis are influenced by the size of MNP. It has been observed that the absorption bands of copper nanoparticles lie between 550 and 600 nm. Figure 3c displays the UV-vis spectra of copper nanoparticles derived from the polymers (PA and PH) in the original reaction mixture. It is evident that the Cu-PH sample has distinct positions for its absorption bands. Smaller nanoparticles are suggested by the absorption peak small shift from 590 to 580 nm for the Cu-PH sample.

A useful tool for measuring particle formation is Fourier Transform Infrared (FTIR) spectroscopy. It is revealed that there is a clear relationship between the particle size and the width and intensity of peaks in an IR spectrum. The width of the peak diminishes, and the intensity increases with increasing particle size. The peaks of the FTIR spectra of Cu nanoparticles in Fig. 3d are visible. The area is bounded by carboxyl or carbonyl groups between 1700–1500 and 1400–1200 cm^{-1}. The transmittance decreases in this area affirms the formation of nanoparticles. The IR spectrum revealed peaks at 1620 cm^{-1} (C=C stretch) and 1210 cm^{-1} (C-O bend), as well as absorptions in the range of 3600–3500 cm^{-1} (N-H stretch), 3300-2600 cm^{-1} (O-H stretch), and 1050-850 cm^{-1} (C-H bend). For Cu NPs produced with polymers present, a comparable explanation was reported [51]. When polymers are present during the

synthesis of Cu NPs, the most distinctive signal indicating their presence could overlap with the polymers.

3.4 Structural, thermal, optical, and chemical properties of Zn nanoparticles

Figure 4a shows the XRD patterns of Zn NPs synthesized from PA and PH. The XRD pattern of Zn-PA exhibited 2θ peaks at around 31°, 36°, and 60°, corresponding to (100), (101), and (110) planes of ZnO, respectively (JCPDS-36-1451) [52]. A peak shift was noted in comparison to the Zn-PH XRD pattern. A shift in the lattice parameters may be the cause of the peak shift. However, the formation of Zn nanoparticles is confirmed in both patterns. The XRD patterns of both PA and PH showed a broad diffraction peak at 26°, which can be attributed to the amorphous nature of polymers. TGA was used to examine the thermal stability of both samples in a N$_2$ environment. TGA curves for Zn-PA and Zn-PH nanoparticle-based samples are shown in Fig. 4b. The TGA curves of the nanoparticles make it clear that the thermal properties of the produced samples are positively impacted by the polymer-based nanoparticles. When it came to thermal stability, the Zn-PA sample outperformed the Zn-PH sample. But in the temperature range up to 250 °C, neither sample showed any appreciable degradations. The homogeneous distribution of ZnO nanoparticles in the PA matrix and the strong adhesion between zinc oxide and the matrix are responsible for the Zn-PA sample's enhanced thermal stability, which has prevented the sample from degrading due to heat. The degradation of polymers may be the cause of the weight loss in both samples at higher temperatures. Figure 4c shows the solution state UV-vis absorption spectra of Zn-PA and Zn-PH PANC. The successful surface modification of ZnO nanoparticles can be inferred from a comparison of the UV-vis spectra of Zn-PA and Zn-PH. The transition of the charge transfer electron at the coordinated sites caused the absorbance peaks of ZnO nanoparticles to appear between 300 and 350 nm. The Zn-PA absorption spectra showed a minor blue shift, which was followed by a shift to the highest absorption peak of ZnO nanoparticles.

This resulted in a decrease in the intensity of the nanocomposite adsorption. ZnO nanoparticle compatibility and excellent distribution within the PH matrix are responsible for a decrease in the intensity of UV absorption for Zn-PH. Figure 4d displays the FTIR spectra of Zn-PA and Zn-PH samples. The hydroxyl groups on the surface of ZnO nanoparticles were identified as the cause of the absorption band at 3480 cm^{-1} in the FTIR spectrum. Following ZnO nanoparticle modification, new, distinctive absorption bands developed at 3044 cm^{-1}, 1650 cm^{-1}, 1480 cm^{-1}, and 1230 cm^{-1}. These bands were associated with the carbon-oxygen bond, the double

Fig. 4 Zinc (Zn) nanoparticles synthesized from polyamide (PA) and polyhydrazide (PH); XRD pattern (**a**), TGA Curves (**b**), UV-VIS spectra (**c**), and IR spectra (**d**)
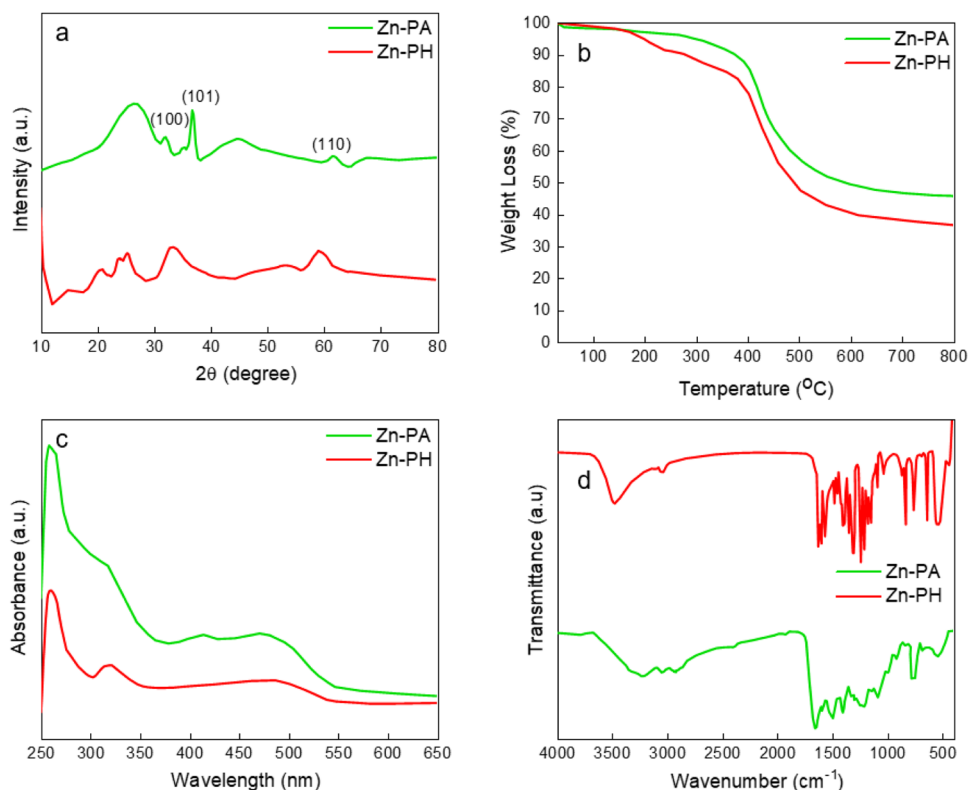
carbon-carbon bands in aromatic rings, and aromatic CH, respectively. The distinctive absorption band, which is associated with the stretching vibration of the carbon-carbon double bond in the polymer chain, first showed at $1590 \, cm^{-1}$. The amide group stretching vibration caused the absorption bands for the carbonyl groups in the nanocomposite FTIR spectra to be $\sim 1660 \, cm^{-1}$. Zn-O in the polymer structure caused the absorption band at $535 \, cm^{-1}$ [53].

3.5 Morphological characteristics of metal nanoparticles

Figure 5 displays the images obtained from the scanning electron microscopy (SEM) analysis of the surface morphology of MNP. The polymer surface exhibits a uniform loading of MNP. The random distribution of nanoparticles was observed with sizes in nanometric dimension. The uniform deposition of silver nanoparticles on the polymer matrix was verified by the Ag nanoparticles shown in Fig. 5a. The agglomerated particles could be explained by the nanoparticles thermo-migration that occurs when they are heated to the boiling point. In Fig. 5b, the Fe nanoparticles displayed a wide size distribution, but Cu nanoparticles in Fig. 5c are primarily spherical, in line with the previously described shape of Cu nanoparticles. The size of the resulting particles increases to roughly 200 nm, and they are

irregular. Bulk morphology Zn nanoparticles exhibit severe aggregation.

3.6 Comparison of metal nanoparticles in polyamide and polyhydrazide matrices

In order to identify the optimal combination for the intended applications, we synthesized Ag, Fe, Cu, and Zn nanoparticles using PA and PH matrices. We then examined their morphological, optical, and functional properties. The nanoparticles produced in both polymers had different morphologies, as seen by SEM. Ag-PH and Ag-PA nanoparticles were both spherical, but Ag-PA had a smaller average size and improved dispersion. The nanoparticles of Fe-PA and Fe-PH had cubic forms, while the size distribution of Fe-PA was more uniform. The majority of Cu-PA and Cu-PH nanoparticles were spherical, while Cu-PH showed reduced aggregation. Zn-PH nanoparticles produced more asymmetrical morphologies, while Zn-PA nanoparticles produced rod-like formations. The production of nanoparticles was confirmed by typical absorption peaks observed in UV-Vis spectroscopy. When compared to Ag-PH (420 nm), Ag-PA nanoparticles' peak at 425 nm was slightly redshifted, suggesting a bigger particle size. Around 400 nm, Fe-PA and Fe-PH showed absorption edges, with Fe-PA exhibiting increased UV absorption. Cu-PH nanoparticles showed a peak at 580 nm, indicating a

Fig. 5 SEM images of metal
nanoparticles; Ag nanoparticles
(**a**), Fe nanoparticles (**b**), Cu
nanoparticles (**c**), and Zn
nanoparticles (**d**)
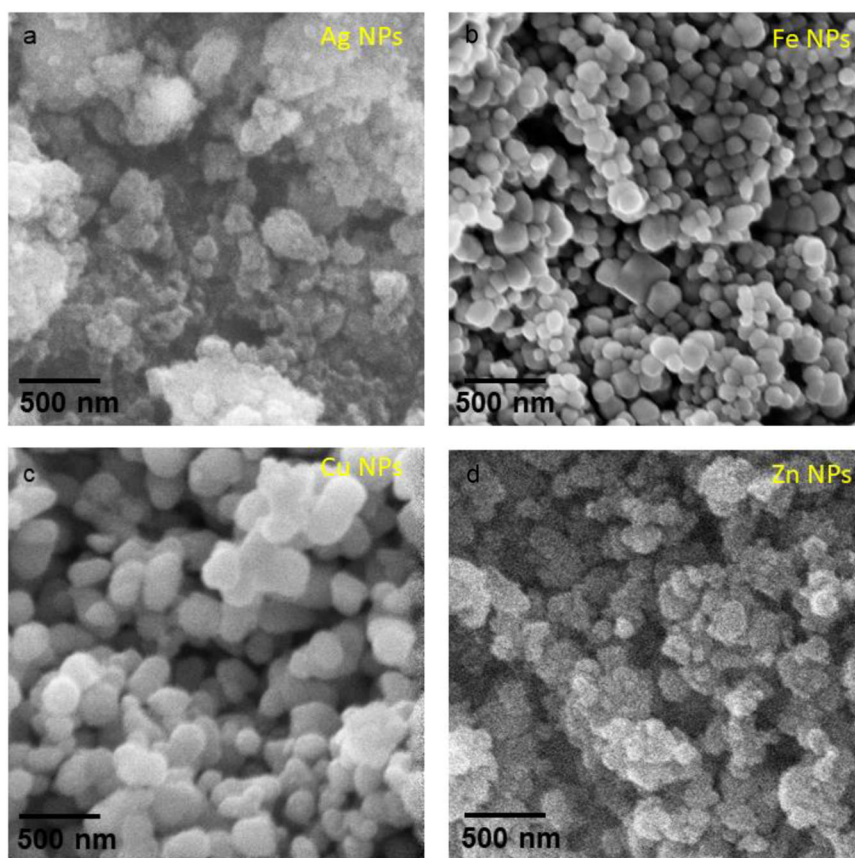
lower particle size than Cu-PA nanoparticles, which produced a peak at 590 nm. Strong UV absorption was observed in Zn-PA and Zn-PH, with Zn-PA showing a minor blue shift, suggesting smaller particle sizes or improved dispersion. The inclusion of MNP into both matrices was successfully demonstrated by FTIR spectroscopy. As a result of the interaction with Ag nanoparticles, Ag-PA displayed distinctive amide group vibrations with shifts. Magnetite generation was confirmed by Fe-O stretching peaks in Fe-PA, while Fe-PH had extra peaks that may have resulted from complexation with hydrazide groups. Cu-O and C=O group peaks were visible in the Cu-PA and Cu-PH spectra, suggesting interaction with the polymer matrix. Zn-O stretching vibrations were seen in Zn-PA and Zn-PH, with Zn-PA displaying fewer extra peaks, indicating less interaction with the polymer matrix. When comparing PA-based nanoparticles to PH-based ones, TGA revealed enhanced heat stability in the former. Because of their stronger connections between the polymer and the nanoparticle, Ag-PA and Fe-PA nanoparticles demonstrated improved thermal stability by exhibiting lower weight loss and higher breakdown temperatures. Because the nanoparticles were more steadily incorporated into the PA matrix, the Cu-PA and Zn-PA samples also showed better thermal characteristics than their PH

counterparts. Ag-PA and Fe-PA combinations stand out as the best choices for applications needing uniform nanoparticle dispersion and high thermal stability, such as in catalysis and electronics, based on size, shape, optical properties, functional group characteristics, and thermal stability. Zn-PA performs better for applications requiring high UV absorption and optical clarity. Hence, to produce MNP in a variety of applications, PA matrices typically offer better overall properties.

4 Conclusion

In summary, we synthesized the MNP (Ag, Fe, Cu, and Zn) from two different kinds of polymers, PA and PH. The synthesized nanoparticles exhibited highly crystalline structures with better thermal stability. The SEM images confirmed the successful formation of nanoparticles. These findings highlight the effectiveness of PA and PH in facilitating the synthesis of distinct MNP, which can be potentially utilized in sensing, biomedical, and catalysis. Finally, the facile approach chemical reduction method for synthesizing MNP from PA and PH offers a strong path forward for the development of nanomaterial synthesis and applications. Only a few metals Ag, Fe, Cu, and Zn were the

focus of the study. Broadening the range of metals used could yield a more thorough understanding of the synthesis method potential and constraints. The synthesized nanoparticles potential uses in practical applications were not thoroughly examined in this study. To evaluate their effectiveness, real-world testing is required in biological, catalytic, and sensing applications. There were two types of polymer matrices used: PA and PH. If alternative polymers are investigated, it might become clear if the benefits noted are unique to ones or more universal. Prospective investigations ought to encompass a more extensive assortment of metals to examine the adaptability and constraints of the synthesis technique utilizing distinct metal kinds. Concerning cost, yield, and process stability, research ought to concentrate on how scalable the synthesis process is to assess its industrial suitability. Experiments with other polymers for nanoparticle synthesis may reveal whether the efficiency of the procedure is limited to PA and PH, or if it may be used to a larger class of polymer matrices.

Author contributions All authors have equal contributions.

Compliance with ethical standards

Conflict of interest The authors declare no competing interests.

References

1. Malik S, Muhammad K, Waheed Y (2023) Nanotechnology: a revolution in modern industry. Molecules 28(2):661
2. Hansen SF, Hansen OFH, Nielsen MB (2020) Advances and challenges towards consumerization of nanomaterials. Nat Nanotechnol 15(12):964–965
3. Manikandan S et al. (2023) Emerging nanotechnology in renewable biogas production from biowastes: Impact and optimization strategies—A review. Renew Sustain Energy Rev 181:113345
4. Song J-H et al. (2022) Multi-functionalization strategies using nanomaterials: a review and case study in sensing applications. Int J Precis Eng Manuf-Green Technol 9(1):323–347
5. Mohamed NA, Selim S, Galal A (2021) Thermal and optical properties of aromatic polyamide–hydrazides modified with multiwalled carbon nanotubes. Polym Polym Compos 29(6):591–604
6. 赵宇宏 et al. (2021) 装甲防护陶瓷-金属叠层复合材料界面研究进展. 金属学报 57(9):1107–1125
7. Jamkhande PG et al. (2019) Metal nanoparticles synthesis: an overview on methods of preparation, advantages and disadvantages, and applications. J Drug Deliv Sci Technol 53:101174
8. Dikshit PK et al. (2021) Green synthesis of metallic nanoparticles: applications and limitations. Catalysts 11(8):902
9. Alrajhi AH, Ahmed NM (2022) Green synthesis of zinc oxide nanoparticles using salvia officinalis extract. In: Shanker U, Hussain CM, Rani M (eds) Handbook of green and sustainable nanotechnology: fundamentals, developments and applications. Springer International Publishing, Cham. p 1–21
10. Fresco-Cala B, Cárdenas S (2022) Advanced polymeric solids containing nano- and micro-particles prepared via emulsion-based polymerization approaches. A review. Anal Chim Acta 1208:339669
11. Madkour M, Bumajdad A, Al-Sagheer F (2019) To what extent do polymeric stabilizers affect nanoparticles characteristics? Adv Colloid Interface Sci 270:38–53
12. Ding H et al. (2023) Achieving strength-ductility synergy in metallic glasses via electric current-enhanced structural fluctuations. Int J Plast 169:103711
13. Durga G et al. (2021) Ionic liquids: from a solvent for polymeric reactions to the monomers for poly(ionic liquids). J Mol Liq 335:116540
14. Jalalvandi E, Shavandi A (2018) Polysuccinimide and its derivatives: degradable and water soluble polymers (review). Eur Polym J 109:43–54
15. Fernandes M et al. (2022) Polysaccharides and metal nanoparticles for functional textiles: a review. Nanomaterials 12(6):1006
16. Guo L et al. (2023) Poly(hydrazide–imide) membranes with enhanced interchain interaction for highly selective H2/CO2 separation. Macromolecules 56(9):3430–3439
17. Khedr MSF (2023) Bio-based polyamide. Phys Sci Rev 8(7):827–847
18. Mishra N, Madhad H, Vasava D (2021) Progress in the chemistry of functional aramids properties. J Heterocycl Chem 58(10):1887–1913
19. Francisco DL, Paiva LB, Aldeia W (2019) Advances in polyamide nanocomposites: a review. Polym Compos 40(3):851–870
20. Parvate S, Mahanwar P (2019) Advances in self-crosslinking of acrylic emulsion: what we know and what we would like to know. J Dispers Sci Technol 40(4):519–536
21. Shekhar S et al. (2023) Sustainable polysaccharide hydrogels based on dynamic schiff base linkages as versatile building blocks for fabricating advanced functional materials. J Polym Environ 31(4):1257–1278
22. Elsabee MZ, Morsi RE, Selim S (2018) High-performance wholly aromatic polyamide–hydrazides: achievements and future prospects. High Perform Polym 30(4):387–405
23. Haque SM et al. (2021) Application and suitability of polymeric materials as insulators in electrical equipment. Energies 14(10):2758
24. Xu J-J et al. (2022) Metal nanoparticles as a promising technology in targeted cancer treatment. Drug Deliv 29(1):664–678
25. Kuang W et al. (2018) Application of the thermodynamic extremal principle to diffusion-controlled phase transformations in Fe-CX alloys: Modeling and applications. Acta Mater 159:16–30
26. Sun M et al. (2022) In-situ polymerization methods for polymer-based solid-state lithium batteries. Batteries Supercaps 5(12):e202200338
27. Vijayakumar V et al. (2021) In situ polymerization process: an essential design tool for lithium polymer batteries. Energy Environ Sci 14(5):2708–2788
28. Zhao Y et al. (2019) Phase-field simulation for the evolution of solid/liquid interface front in directional solidification process. J Mater Sci Technol 35(6):1044–1052
29. Liu K et al. (2022) Triarylboron-doped acenethiophenes as organic sonosensitizers for highly efficient sonodynamic therapy with low phototoxicity. Adv Mater 34(49):2206594
30. Zhu Q et al. (2017) Ameliorated longitudinal critically refracted—attenuation velocity method for welding residual stress measurement. J Mater Process Technol 246:267–275

31. He Y et al. (2024) Study on the atomic removal behavior and damage formation mechanism of nano cutting copper–nickel alloy with diamond tool. Model Simul Mater Sci Eng 32(3):035011

32. Kaur A et al. (2022) A review on template assisted synthesis of multi-functional metal oxide nanostructures: status and prospects. Mater Sci Eng: B 286:116005

33. Poolakkandy RR, Menamparambath MM (2020) Soft-template-assisted synthesis: a promising approach for the fabrication of transition metal oxides. Nanoscale Adv 2(11):5015–5045

34. Das TK et al. (2021) Efficient synthesis of catalytic active silver nanoparticles illuminated cerium oxide nanotube: a mussel inspired approach. Environ Nanotechnol Monit Manag 15:100411

35. Das TK et al. (2020) Mussel-inspired Ag/poly(norepinephrine)/MnO$_2$ heterogeneous nanocatalyst for efficient reduction of 4-nitrophenol and 4-nitroaniline: an alternative approach. Res Chem Intermed 46(7):3629–3650

36. Daruich De Souza C, Ribeiro Nogueira B, Rostelato MECM (2019) Review of the methodologies used in the synthesis gold nanoparticles by chemical reduction. J Alloy Compd 798:714–740

37. Chandrakala V, Aruna V, Angajala G (2022) Review on metal nanoparticles as nanocarriers: current challenges and perspectives in drug delivery systems. Emergent Mater 5(6):1593–1615

38. Das TK et al. (2018) A facile green synthesis of silver nanoparticle-decorated hydroxyapatite for efficient catalytic activity towards 4-nitrophenol reduction. Res Chem Intermed 44(2):1189–1208

39. Kanti Das T et al. (2019) Temperature-dependent study of catalytic Ag nanoparticles entrapped resin nanocomposite towards reduction of 4-nitrophenol. ChemistrySelect 4(13):3665–3671

40. Salam MA et al. (2017) Synthesis of nanocomposites of polypyrrole/carbon nanotubes/silver nano particles and their application in water disinfection. RSC Adv 7(27):16878–16884

41. Li C-P, Chen J, Du M (2010) Structural diversification and metal-directed assembly of coordination architectures based on tetra-bromoterephthalic acid and a bent dipyridyl tecton 2,5-bis(4-pyridyl)-1,3,4-oxadiazole. CrystEngComm 12(12):4392–4402

42. de Souza MGM et al. (2022) Silver nanoparticle incorporation into flexible polyamide 12 membranes. J Sol-Gel Sci Technol 102(1):219–228

43. Montazer M, Shamei A, Alimohammadi F (2014) Synthesis of nanosilver on polyamide fabric using silver/ammonia complex. Mater Sci Eng: C 38:170–176

44. Cheval N et al. (2012) Polyamide 66 microspheres metallised with in situ synthesised gold nanoparticles for a catalytic application. Nanoscale Res Lett 7(1):182

45. Abdel Aziz WN et al. (2020) Selective synthesis and characterization of iron oxide nanoparticles via PVA/PVP polymer blend as structure-directing agent. Mater Chem Phys 249:122927

46. Majó MA et al. (2004) Synthesis and characterization of polyamides obtained from tartaric acid and l-lysine. Eur Polym J 40(12):2699–2708

47. Liang Y et al. (2007) Synthesis and performances of Fe2O3/PA-6 nanocomposite fiber. Mater Lett 61(14):3269–3272

48. Pasinszki T, Krebsz M (2020) Synthesis and application of zero-valent iron nanoparticles in water treatment, environmental remediation, catalysis, and their biological effects. Nanomaterials 10(5):917

49. Xu Q et al. (2019) Preparation of polyamide 6/copper nanocomposites and its properties. Rev Roum Chim 64(6):479–484

50. Deng D et al. (2012) Antioxidative effect of lactic acid-stabilized copper nanoparticles prepared in aqueous solution. J Mater Chem 22(45):23989–23995

51. Jardón-Maximino N et al. (2021) Synthesis of copper nanoparticles stabilized with organic ligands and their antimicrobial properties. Polymers 13(17):2846

52. Jeeju PP et al. (2013) Enhanced linear and nonlinear optical properties of thermally stable ZnO/poly(styrene)–poly(methyl methacrylate) nanocomposite films. Thin Solid Films 531:378–384

53. Hajibeygi M et al. (2017) Optical, thermal and combustion properties of self-colored polyamide nanocomposites reinforced with azo dye surface modified ZnO nanoparticles. Appl Surf Sci 416:628–638